



Redirecting the route: Monocyte-mediated delivery of oHSV-1 across a human BBB-on-chip model

Sara Micheli^{a,b,1} , Alberto Reale^{c,1} , Alessandra Rossetto^c, Cristina Parolin^c, Fabio Mammano^{d,e} , Arianna Calistri^{c,*}, Elisa Cimetta^{a,b,**}

^a Department of Industrial Engineering, University of Padua, Padua, Italy

^b Fondazione Istituto di Ricerca Pediatrica Città della Speranza, Padua, Italy

^c Department of Molecular Medicine, University of Padua, Italy

^d Department of Physics and Astronomy "G. Galilei", University of Padua, Padua, Italy

^e CNR Institute of Biochemistry and Cell Biology, Monterotondo, Rome, Italy

ARTICLE INFO

Keywords:

BBB-On-chip

Glioblastoma spheroids

Monocytes

Oncolytic HSV-1

ABSTRACT

Oncolytic viruses (OVs) that selectively replicate within cancer cells represent a promising therapeutic strategy for refractory or difficult-to-treat tumors such as Glioblastoma (GBM). In this study, we develop and validate a human microfluidic blood brain barrier (BBB) model to evaluate the potential of cell-based OVs delivery targeting the central nervous system. We demonstrate that circulating leukocytes (monocytes), serve as effective carrier cells for the delivery of a neuroattenuated strain of oncolytic herpes simplex virus type 1 (oHSV-1) to GBM. Human monocytes infected with oHSV-1 and perfused through the device successfully traverse the BBB and migrate toward human GBM spheroids, where they deliver the virus and initiate infection. Notably, monocyte-mediated oHSV-1 delivery to the tumor occurs with **minimal involvement of BBB infection** and remains effective even in the presence of anti-HSV-1 antibodies, commonly found in the general population. In contrast, free oHSV-1 infects BBB-resident cells and is neutralized by circulating human immunoglobulins. These findings highlight the potential of monocyte-based oHSV-1 delivery as a targeted, immune-shielded strategy for GBM therapy.

1. Introduction

The blood–brain barrier (BBB) is a specialized anatomical structure composed of vascular endothelial cells, pericytes, and astrocytes that selectively filter molecules from the bloodstream into the central nervous system (CNS) [1]. As such, the BBB poses a significant challenge for the pharmacological treatment of CNS diseases [2] such as glioblastoma (GBM) [3]. GBM is the most common primary brain tumor in adults [4] and carries a very dismal prognosis [5]. Despite some progress with chimeric antigen receptor (CAR)-T cell therapies, immunotherapy remains largely ineffective against GBM [6,7]. This is due to multiple factors including inactivation by the tumor microenvironment, target antigen heterogeneity, and limited trafficking across the BBB, often necessitating intraventricular administration [8,9].

Oncolytic viruses (OVs) are naturally occurring or engineered viruses

that selectively replicate in cancer cells by exploiting deficiencies in antiviral defense pathways [10]. These agents offer a multifaceted therapeutic approach that includes direct tumor lysis, immune activation, and gene delivery [11]. While talimogene laherparepvec (T-VEC), an oHSV-1-based OV, is approved for the treatment of melanoma [12], another oHSV-1 has recently been authorized in Japan for GBM following promising clinical trials [13]. Effective OV delivery to GBM remains a challenge. Intracranial injection, although effective, is invasive and not easily repeatable. Moreover, GBM's invasive nature and tendency to recur in distant brain areas make localized therapy insufficient. Intravenous administration is hindered by the BBB and by neutralization of circulating virions, particularly in the case of HSV-1, due to widespread pre-existing immunity in the population [14]. Carrier cells provide a potential solution. These include mesenchymal stromal cells (MSCs) [15] and immune cells such as monocytes, which

* Corresponding author.

** Corresponding author. Department of Industrial Engineering, University of Padua, Padua, Italy.

E-mail addresses: arianna.calistri@unipd.it (A. Calistri), elisa.cimetta@unipd.it (E. Cimetta).

¹ Those Authors contributed equally to the work.

we identified as suitable carriers for oHSV-1 [16]. We previously demonstrated that monocytes are susceptible to infection by an oHSV-1 closely resembling the clinically approved T-VEC. THP-1 cells, derived from monocytic leukemia, supported productive infection, while primary monocytes from healthy donors, although susceptible, were only poorly permissive to viral replication [16]. Despite low permissiveness, most infected primary monocytes expressed the immediate early viral protein ICP4 and, upon exposure to tumor cell-conditioned medium, showed a significant increase in viral particle production. Infected monocytes retained their ability to migrate toward tumor-derived signals and successfully transmitted the virus to tumor cells in co-culture experiments. Furthermore, using the chorioallantoic membrane (CAM) model, we confirmed that oHSV-1-loaded THP-1 cells were capable of homing to and infecting vascularized tumors within the developing chicken embryo [16]. Taken together, these preliminary findings support the potential of monocytes as cellular carriers for oncolytic virotherapy, for their efficient *ex vivo* loading and natural tumor tropism to facilitate delivery of the viral payload while evading immune clearance.

Replicating the BBB *in vitro* poses challenges due to its complex cellular architecture. While *in vivo* studies offer physiological insights, they are limited by interspecies differences, ethical constraints, and scalability [17,18]. Traditional static *in vitro* models fall short due to lack of shear stress and incomplete cellular interactions [19,20]. Researchers developed BBB-on-chip systems, microfluidic platforms designed to replicate physiological and functional aspects of the BBB *in vitro* [21]. Microfluidic BBB devices offer numerous advantages for *in vitro* modeling, making them an ideal alternative to traditional systems [17]. They are cost-effective to fabricate and provide flexibility in design, allowing to tailor the setup to specific experimental needs. These devices require fewer cells, increase efficiency and reduce materials consumption [22]. By offering precise control over the microenvironment, microfluidic systems can more closely replicate the actual *in vivo* brain anatomy and physiology, including critical factors such as shear stress [23]. The ability to measure relevant parameters such as BBB permeability in real time, enhances both the speed and accuracy of data collection, while improving paracellular barrier functions. Additionally, the transparent nature of the devices allows for easy cell inspection via microscopy. With the possibility of integrating co-culture models, these platforms offer a more realistic simulation of the cellular interactions that occur within the brain, further advancing the physiological relevance of BBB modeling [24,25]. Overall, microfluidic BBB models provide a promising alternative to traditional *in vitro* cell cultures and animal experimentation, offering the potential for more accurate and realistic BBB modeling.

In the context of GBM, the cerebral vasculature undergoes significant remodeling, giving rise to what is commonly referred to as the blood-brain tumor barrier (BBTB). Although the BBTB exhibits increased permeability due to neovascularization and inflammation, it retains regions with intact BBB characteristics and displays heterogeneity across the tumor microenvironment (TME). [26] Overexpression of vascular endothelial growth factor (VEGF) in GBM downregulates tight junction proteins such as claudin-5 and occludin, resulting in endothelial hyperpermeability and structural disruption of the barrier. [27] Despite being more permeable than the healthy BBB, the BBTB remains highly variable in both perfusion and permeability, leading to inconsistent drug accumulation and presenting a major obstacle to effective therapeutic delivery [28,29]. For this reason, *in vitro* models that preserve the structural and functional integrity of the healthy BBB are crucial for investigating early tumor-vascular interactions and drug transport mechanisms under controlled conditions. In this study, we developed a tri-compartmental BBB-on-chip platform composed of endothelial, astrocytic, and pericytic layers, to which a GBM compartment is connected. GBM spheroids were introduced only after the formation of a mature and stable BBB, closely mimicking the transition from a healthy to a tumor-altered barrier. This configuration enables the dynamic study of GBM-induced

barrier disruption while preserving physiologically relevant baseline conditions. Using this model, we demonstrated that monocytes can efficiently traverse the BBB and deliver oHSV-1 to GBM spheroids, even in the presence of neutralizing antibodies, further highlighting the potential of this approach for overcoming key limitations in drug delivery to brain tumors.

2. Results and discussion

2.1. A microfluidic BBB-on-chip model allows growth of multiple cell types and BBB-like permeability

The BBB-on-chip was designed with a structure consisting of three distinct layers, to replicate the BBB microenvironment and incorporate a 3D GBM tumor culture for advanced cancer modeling (Fig. 1). Each compartment serves a specific role in mimicking the physiological interactions between the blood and brain regions. The apical compartment, highlighted in yellow in Fig. 1A, represents the blood-facing side of the BBB. This layer enables the perfusion of culture medium and soluble species, simulating blood flow above the barrier. Continuous perfusion creates dynamic conditions critical for evaluating the transport and permeability of molecules across the BBB. The membrane layer, shown in black in Fig. 1A, has a support role and mimics the selective barrier properties of the BBB. The membranes used are made of transparent polyester (PETE) with a 3 μm pore diameter. The basolateral compartment, marked in red in Fig. 1A, represents the brain-facing side of the BBB. This compartment includes a tumor area composed of three microwells designed to accommodate 3D spheroids (red dashed box in Fig. 1B). The inclusion of the tumor compartment provides a physiologically relevant microenvironment to study tumor-BBB interactions, drug penetration, and spheroid behavior under perfused conditions.

Stable co-culture within the BBB-on-chip follows an optimized sequential seeding protocol to ensure the proper attachment and viability of all cell lines. Astrocytes and pericytes are first seeded on the basolateral side of the porous PETE membrane and then incubated overnight to facilitate adhesion. The following day, human umbilical vein endothelial cells (HUVECs) are seeded on the apical side to complete the BBB structure. Live/Dead assay results, presented in Supplementary Figure S1, demonstrate successful attachment and high viability of all cell types on their respective side of the PETE membrane. These findings confirm that the seeding protocol and microenvironment within the BBB-on-chip are suitable for the growth and maintenance of the three-culture model.

Based on the results of numerical simulations, the cell culture medium perfusion flow rate through the blood side (Inlet/Outlet 2 in Fig. 1B) is set to 30 $\mu\text{L}/\text{min}$, corresponding to a shear stress at the bottom wall of $\sim 7 \text{ dyne}/\text{cm}^2$ (see Supplementary Figure S2 for additional details). This value falls within the physiological shear stress range reported in the literature for blood vessels, which is between 3 and 25 dyne/cm^2 [30] and plays a critical role in maintaining BBB integrity and function. Physiological shear stress levels are also essential for regulating endothelial cell function, promoting barrier tightness, and facilitating proper nutrient and waste exchange.

After seeding, the maturation of the barrier in the microdevices was monitored over the course of 7 days, performing daily Transendothelial Electrical Resistance (TEER) measurements using a voltohmmeter (Fig. 1C). TEER values progressively increase over time, peaking at approximately 340 Ωcm^2 on day 7, indicating the successful formation and maturation of the barrier, consistently with available literature data for comparable on-chip systems [31].

After 7 days of perfused culture, the identity of cells growing on both sides of the membrane was confirmed by immunofluorescence (IF). Specifically, we detected platelet and endothelial cell adhesion molecule 1 (PECAM, or CD31) and zonula occludens-1 (ZO-1) in the endothelial layer of the membrane. Both proteins are involved in endothelial cell junctions and ZO-1 plays a prominent role in the formation of tight

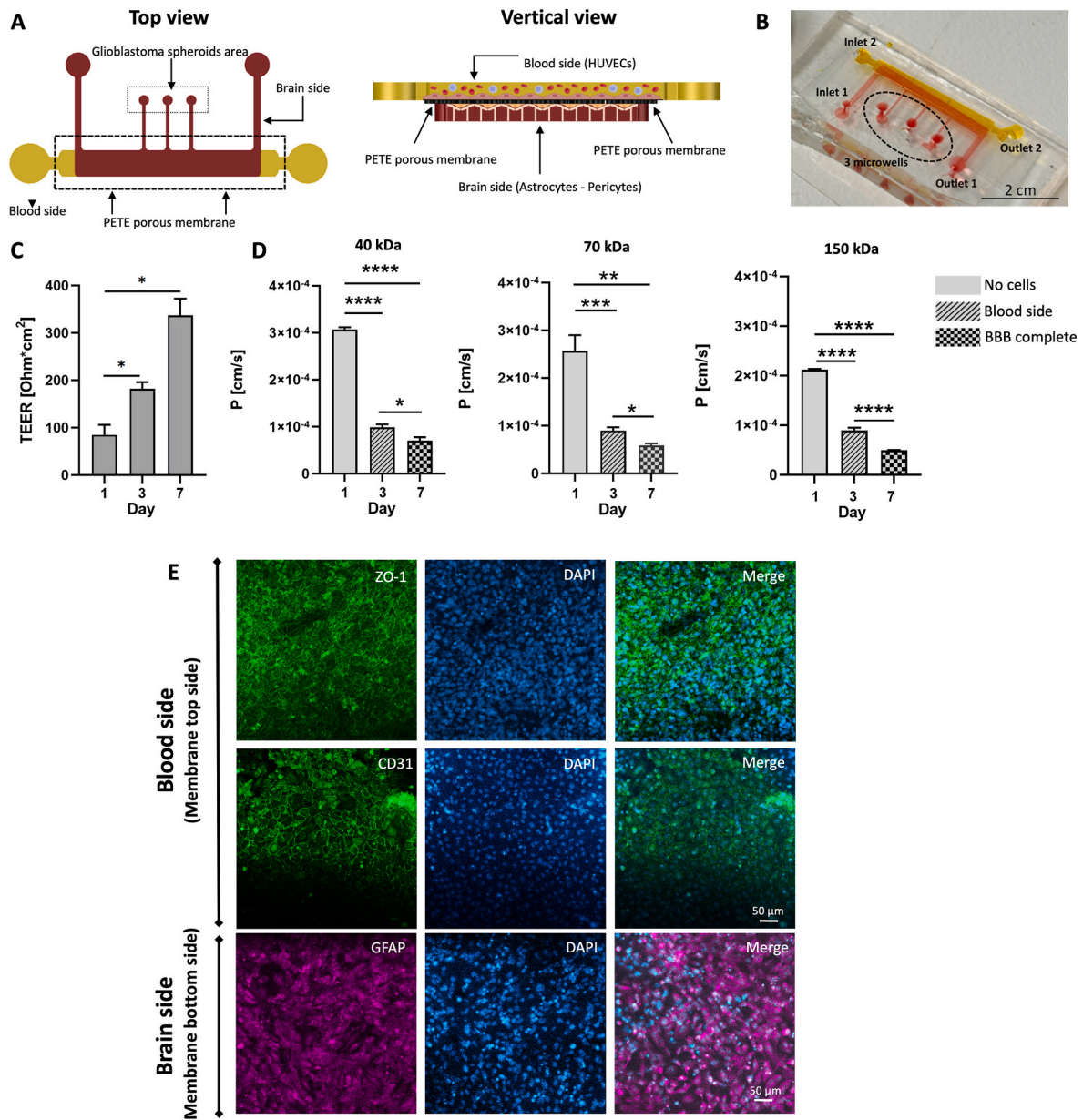


Fig. 1. Microfluidic BBB-on-chip design and validation. **A.** Schematic representation of the BBB-on-chip, seeded with endothelial cells on the blood side and pericytes and astrocytes on the brain side, equipped with three microwells for 3D GBM spheroid culture (GBM spheroids area). **B.** Image of the assembled BBB-on-chip showing the upper channel (yellow) mimicking the vascular compartment and main perfusion conduit, and the lower channels (red) leading to the tumor compartment (scale bar = 2 cm). **C.** Transendothelial electrical resistance (TEER) measurements recorded daily across the membrane between the upper and lower channels and supporting the BBB. **D.** Permeability coefficients calculated from the diffusion of 40, 70, and 150 kDa FITC-dextran through the assembled BBB-on-chip in the following conditions: i. No cells (control, membrane without cells), ii. Blood side (membrane + HUVECs endothelial monolayer), and iii. BBB complete (membrane with the three-culture of HUVECs on the blood side and pericytes and astrocytes on the brain side). **E.** IF staining of the BBB-on-chip model on day 7. On the **blood side compartment**, endothelial tight junction protein ZO-1 (green) and the endothelial marker CD31 (green) are expressed, confirming the formation of a continuous endothelial layer. On the **brain side**, astrocytes are identified by GFAP expression (magenta), indicating appropriate localization. DAPI (blue) highlights cell nuclei in both compartments. Scale bar = 50 μm . Values are expressed as median \pm SEM from at least 3 independent experiments. * $p < 0.05$, ** $p < 0.01$ and *** $p < 0.001$ vs control. (For interpretation of the references to colour in this figure legend, the reader is referred to the Web version of this article.)

junctions, fundamental for BBB function. On the brain side of the barrier, we detected glial fibrillary acidic protein (GFAP), a widely used marker for astrocytes (Fig. 1E). Astrocytes are critical in maintaining BBB integrity by regulating tight junction formation, providing metabolic support, and modulating the selective permeability of the barrier [32]. Combined with the observed TEER increase, these results confirm the successful recreation of a functional BBB-like barrier within the microdevices.

We also tested the ability of our BBB model to restrict molecular

diffusion using FITC-conjugated dextrans in a permeability assay. Dextrans of different molecular weights (40, 70, and 150 kDa) are perfused through the apical (blood channel) side of the device at a flow rate of 5 $\mu\text{L}/\text{min}$. Fluorescence intensity is monitored in the tumor area across the three microwells using a fluorescence microscope with a 488 nm filter, and mean intensity values from specific regions of interest (ROI) are quantified with ImageJ software. To address the role of each cell type in determining the physiological compliance of the barrier after 7 days of perfused culture, we tested the permeability in: i. control devices

without cells, *ii.* devices seeded with a HUVECs monolayer only, and *iii.* the complete BBB model incorporating HUVECs, astrocytes, and pericytes. Representative permeability values are shown in Fig. 1D and demonstrate a clear correlation between dextran molecular weight and diffusion resistance. Higher molecular weight dextrans (70, 150 kDa) accumulate more slowly in the microwells across all experimental conditions, reflecting increased difficulty in crossing the barrier. As expected, control devices without cells show the highest permeability. Introducing a HUVEC monolayer significantly reduced permeability, further decreasing with the addition of astrocytes and pericytes. These findings demonstrate that the inclusion of astrocytes and pericytes significantly improves barrier selectivity, recapitulating the tight junctions organization and restrictive transport properties of the *in vivo* BBB. The progressive decrease in permeability correlates with the expected physiological role of these cell types in regulating molecular transport and maintaining BBB integrity.

2.2. THP-1 cells transmit oHSV-1-mCherry to U87-derived spheroids, with infection leading to decreased viability in cancer cells

The growth and morphological characteristics of spheroids derived from human GBM U87 cells (U87-MG, ATCC) are monitored over the course of 7 days. Brightfield images are captured with optimal contrast and analyzed using AnaSP software to quantify parameters such as equivalent diameter, solidity, compactness and sphericity index (SI). The equivalent diameter of the spheroids increases from approximately 200 μm on day 2–700 μm on day 7, with some growing up to 800 μm (Fig. 2A). Solidity also increases over time, correlating with shape regularity, while compactness decreases due to growth-related effects. The

maintenance of a spherical shape is confirmed by a stable SI ~ 1 throughout the observation period. Fig. 2B reports representative images for Phalloidin/DAPI staining and Live/Dead assay at day 7. To capture the 3D structure of the spheroid, sequential images focus on the outer (shell) and inner (core) sections. Phalloidin/DAPI staining shows well-structured actin filaments and organized nuclei, reflecting proper cellular architecture and spatial arrangement within the spheroids. The Live/Dead assay demonstrates consistent high cell viability.

To explore the potential use of monocytes as carrier cells for the systemic delivery of an HSV-1 based OV, we assess the ability of human monocytic THP-1 cells to transmit a neuroattenuated oHSV-1 expressing a red fluorescent reporter (oHSV-1-mCherry) to GBM spheroids in standard multiwell culture settings. U87-derived spheroids are co-cultured with *i.* uninfected THP-1 cells labeled with CellTracker™ Green (Invitrogen™, Thermo Fisher Scientific), *ii.* labeled THP-1 infected with oHSV-1-mCherry at the multiplicity of infection (MOI) of 3 plaque forming units (PFU)/cell, and *iii.* free oHSV-1-mCherry. Monitoring the spheroids over several days using confocal microscopy enables evaluation of the spreading of the viral infection via mCherry fluorescence visualization. Images in Fig. 2C are representative of GBM spheroids on day 7 post treatment with THP-1 monocytes labeled in green and infected with oHSV-1-mCherry. The fluorescence images illustrate the widespread distribution of oHSV-1-mCherry infected cells (red) and of the carrier THP-1 cells (green) within the GBM spheroids. The same tumor spheroids are tested with a viability MTT assay. On day 7 post-infection (Fig. 2D), the viability of spheroids is significantly reduced both after infection with the free virus and after incubation with oHSV-1-mCherry infected THP-1 cells, indicating an active replication of the virus in cancer cells, independently from the route of

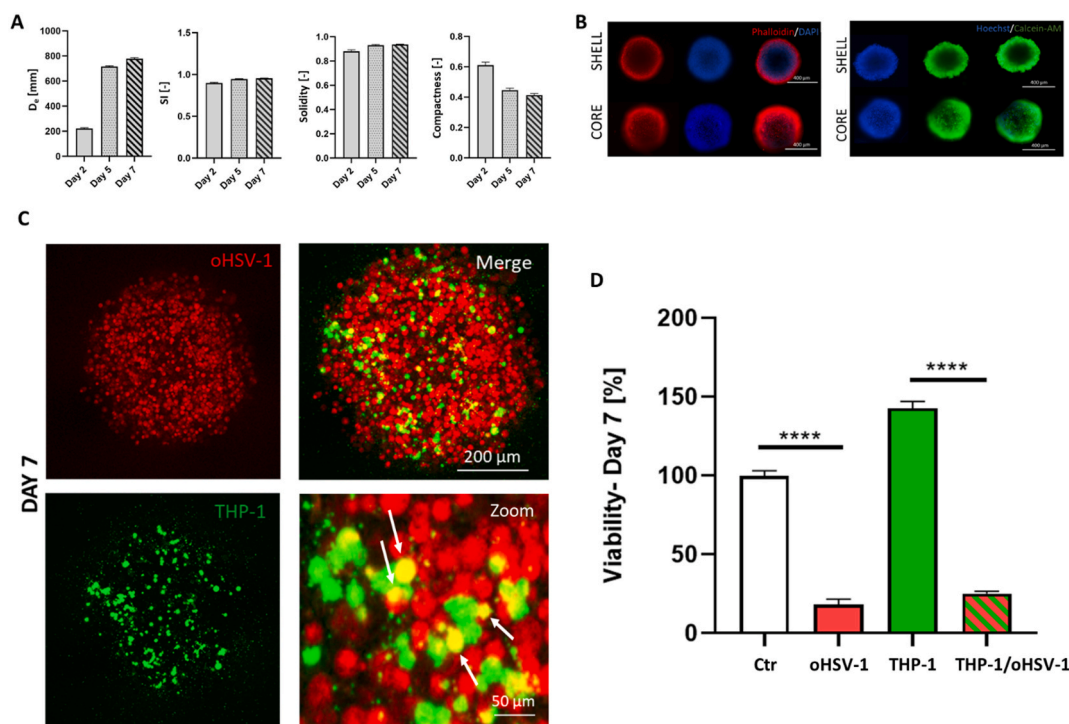


Fig. 2. THP-1 cells deliver oHSV-1 to U87-MG spheroids and the infection decreases tumor cells viability. **A.** Spheroid characterization showing time course AnaSP measurements of: Equivalent diameter (D_e), Sphericity Index (SI), Solidity, and Compactness. **B.** Representative phalloidin + DAPI staining (left) and Live/Dead assay (right) on day 7. F-actin filaments are marked red and cell nuclei blue, showing a correct distribution throughout the 3D structure. Cell viability is consistently high in both the shell and core of the spheroids, with cell nuclei marked in blue with Hoechst and cytoplasm of living cells marked in green with Calcein-AM. Scale bars 400 μm . **C.** U87-MG spheroids treated with THP-1 cells infected at MOI of 3 PFU/cell and labeled with CellTracker™ Green (500 cells/well). On day 7, the red signal of the encoded mCherry protein proves that viral infection propagated throughout the entire spheroid. In the zoomed view, arrows highlight yellow cells, representing infected monocytes in which viral replication is occurring. **D.** MTT assay at day 7. Values are expressed as median \pm SEM from at least 3 independent experiments. ****p < 0.0001 vs control. (For interpretation of the references to colour in this figure legend, the reader is referred to the Web version of this article.)

administration. Of note, the viability of the sample containing GBM cells co-cultured with naïve THP-1 cells (labeled “THP-1” in the graph) appears higher than the control, as the latter does not include THP-1 cells. Given their malignant origin, THP-1 cells are proliferative and metabolically active, thus contributing to the overall increase in measured viability. Overall, these findings support the feasibility of using monocytes as carrier cells for the delivery of oHSV-1 to GBM cells.

2.3. Perfused THP-1 cells loaded with oHSV-1-mCherry cross the BBB and transmit the viral infection to U87-derived tumor spheroids

The BBB-on-chip devices containing U87 GBM spheroids (one per microwell, for a total of three spheroids per device) are connected to the perfusion system on the blood side to deliver: *i.* THP-1 cells labeled with

CellTracker™ Green and infected with oHSV-1-mCherry, *ii.* Uninfected, labeled THP-1 cells, or *iii.* free oHSV-1-mCherry. Negative controls are performed perfusing culture media only. Each device is maintained in perfused conditions and analyzed over several days using fluorescence microscopy to evaluate monocyte migration across the BBB and the transmission and spreading of the viral infection to the tumor spheroids.

First, green-labeled THP-1 monocytes can be detected in the apical compartment (blood side), and as early as after 24 h successfully cross the BBB and are found in the microchannel and in the microwells containing the U87 GBM spheroids (Fig. 3A). Analyzing the tumor compartment with the GBM spheroids (Fig. 3B), fluorescent signals are detected after 24 h, representative of THP-1 cells (green) and virally infected cells (red), further confirming successful crossing of the BBB and targeted migration towards the tumor spheroids. At the later time

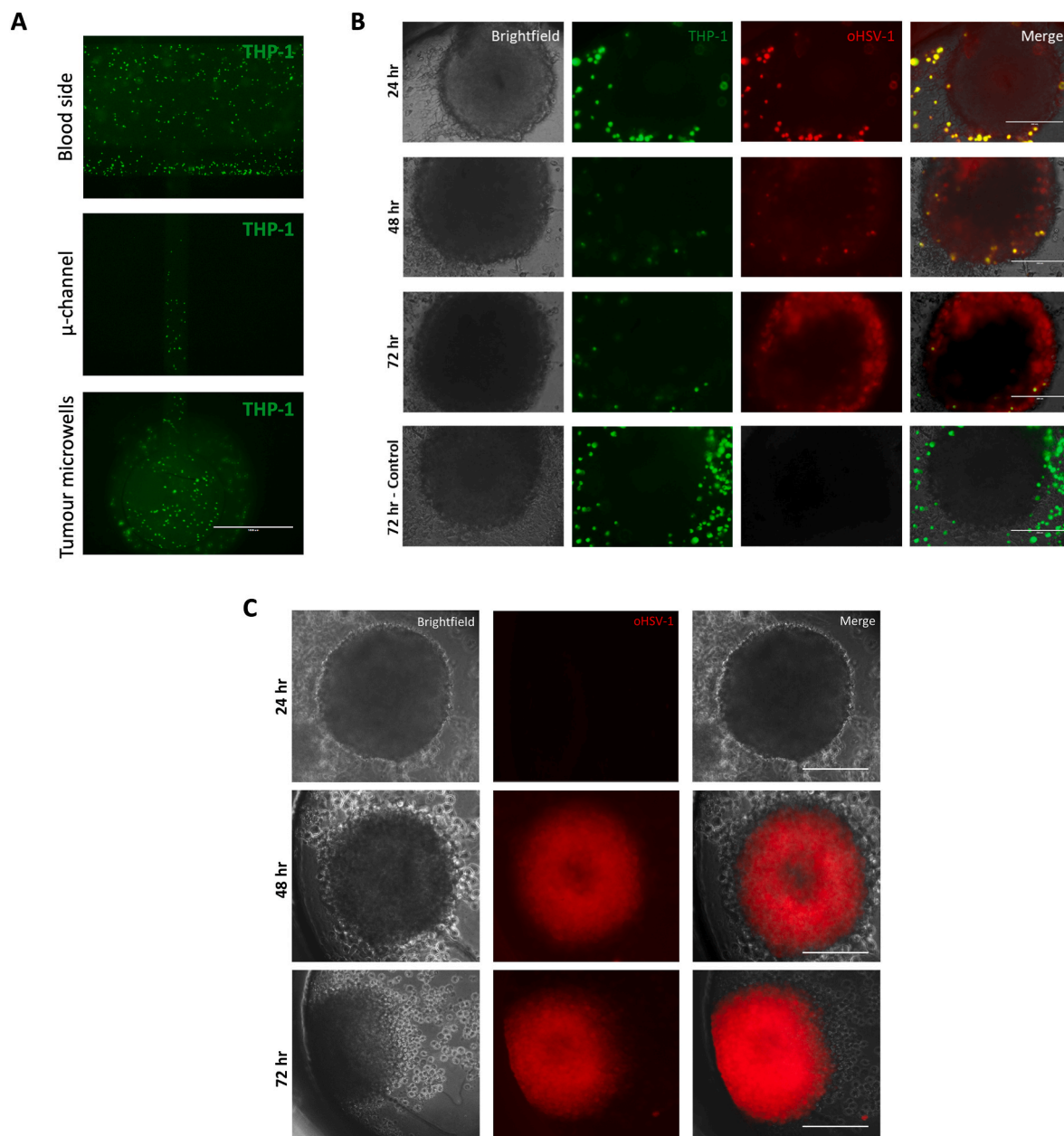


Fig. 3. THP-1 cells cross the BBB-on-chip and deliver oHSV-1 to GBM tumor spheroids. **A.** The BBB-on-chip model is perfused with naïve THP-1 cells marked with CellTracker™ Green (5×10^5 cells/chip). After 24 h, THP-1 cells crossing the BBB reach the GBM spheroids in the microwells of the tumor compartment. **B.** U87 GBM spheroids within the BBB-on-chip perfused with THP-1 cells labeled with CellTracker™ Green and infected with oHSV-1-mCherry (MOI = 3 PFU/cell, 5×10^5 cells/chip), after 24, 48, and 72 h. **C.** U87 GBM spheroids within the BBB-on-chip after perfusion with free oHSV-1-mCherry (1.5×10^6 PFU/chip) after 24, 48, and 72 h. Scale bar: 200 μ m. (For interpretation of the references to colour in this figure legend, the reader is referred to the Web version of this article.)

points of 48 and 72 h, THP-1 cells infected with oHSV-1-mCherry penetrate the tumor spheroids, further transmitting the virus to cancer cells. Free oHSV-1-mCherry viral particles similarly reach the microwells and infect the spheroids, as reported in Fig. 3C. After 72 h, uninfected THP-1 cells continue to proliferate, as reflected by the higher number of green cells observed in the control panels of Fig. 3B. In contrast, this number is notably reduced in the case of infected THP-1 cells, likely because of the cytopathic effects of viral replication, impacting carrier cells viability. Overall, our data show that infected THP-1 cells successfully transmigrate across the BBB and deliver the virus to tumor spheroids, providing a targeted delivery route.

2.4. Human primary monocytes transmit oHSV-1-mCherry infection to GBM spheroids and cross the BBB in the microfluidic model

Building on the successful transmission of oHSV-1-mCherry infection by THP-1 cells to U87 GBM spheroids, we further challenged our model using human primary monocytes from healthy donors, as a more physiologically relevant source for carrier cells. Human primary monocytes isolated from healthy donors are labeled with CellTracker™ Green and loaded with oHSV-1-mCherry, at the same MOI used for the infection of

THP-1 cells (MOI = 3 PFU/cell). First, to assess whether primary monocytes can effectively deliver their viral payload to tumor cells, we co-cultured oHSV-1-mCherry-loaded monocytes with U87 GBM spheroids in standard microwell conditions. Within 24 h (Supplementary Figure S3A), the monocytes successfully migrate toward and infiltrate the spheroids, accumulating both at the tumor periphery and in the core. By 48 h, active viral replication becomes evident, and by day 7, red fluorescence from oHSV-1-mCherry is distributed throughout the 3D tumor spheroid. At this stage, spheroids treated with oHSV-1-loaded primary monocytes display a pronounced reduction in viability compared to untreated controls (Supplementary Figure S3B).

These findings demonstrate that a 3 PFU/cell MOI is suitable for loading primary human monocytes with oHSV-1-mCherry and that these cells, like THP-1 cells, can effectively deliver their payload to GBM spheroids, exerting potent oncolytic activity. The ability of oHSV-1-loaded primary monocytes to cross the BBB and transmit viral infection to U87 GBM spheroids was further assessed using the BBB-on-chip model. Fig. 4A shows the effects on the BBB of oHSV-1, both free and carried by human primary monocytes, perfused for 48 h from the blood side of the device. In the negative control (top row), red fluorescence is absent, and BBB architecture remains intact. When oHSV-1 is delivered

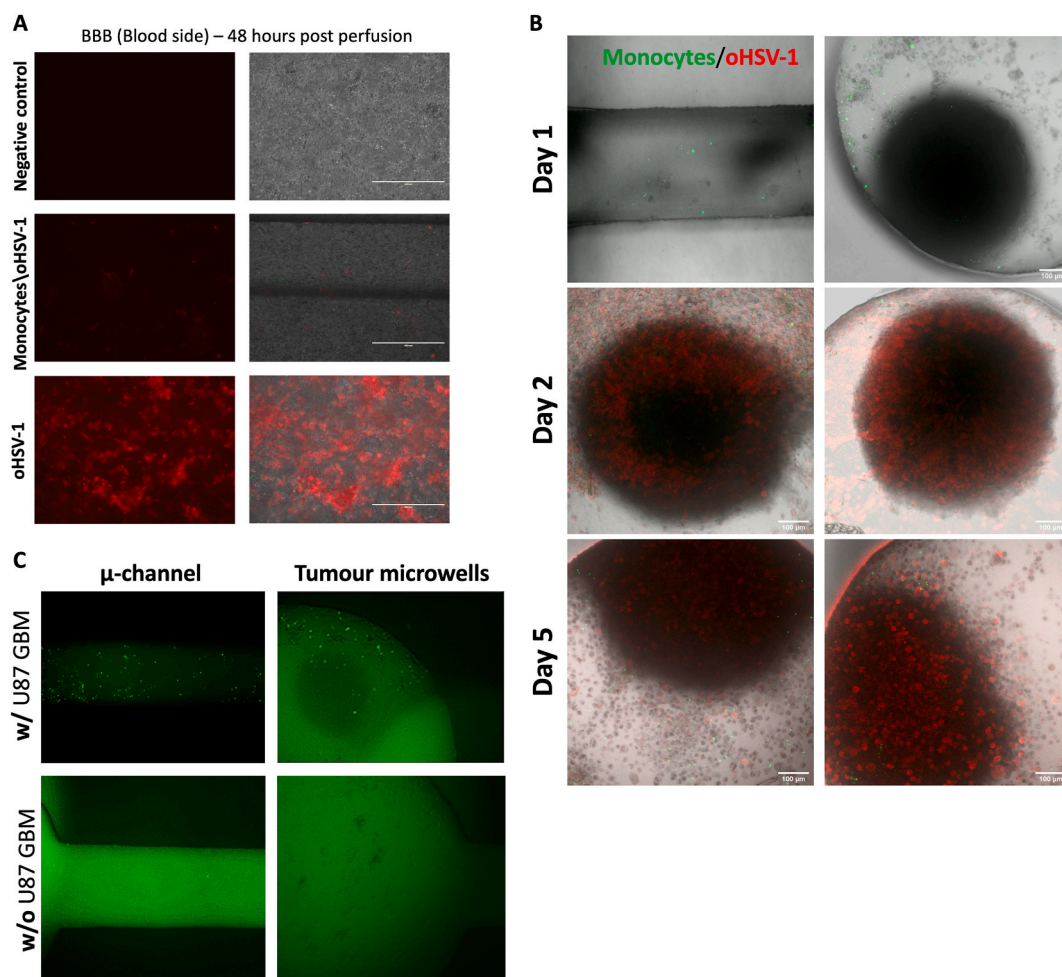


Fig. 4. oHSV-1-loaded human primary monocytes cross the BBB-on-chip and deliver their viral cargo to GBM tumor spheroids. **A.** Representative images of the BBB after 48 h of perfusion with: *i.* cell culture medium (negative control), *ii.* human primary monocytes infected with oHSV-1-mCherry, and *iii.* free virus. While free virus results in strong red fluorescence throughout the barrier region, indicating widespread infection, monocyte-delivered virus shows limited red signal, consistent with preserved BBB integrity. Scale bar: 200 μm. **B.** After 24 h of perfusion, oHSV-1-mCherry-loaded human monocytes cross the BBB and localize within the tumor microwells. At 48 h and day 5, increasing red fluorescence within U87 GBM spheroids indicates progressive viral replication and tumor cell infection. **C.** Monocyte transmigration across the BBB is enhanced in the presence of U87 GBM spheroids. Devices with tumor spheroids exhibit greater numbers of green-labeled monocytes in the microchannel and tumor compartment compared to devices lacking tumor spheroids, suggesting chemotactic recruitment from the TME. (For interpretation of the references to colour in this figure legend, the reader is referred to the Web version of this article.)

via primary monocytes (middle row), only low levels of red fluorescence are detected, indicating minimal interaction with BBB-associated cells and preservation of barrier integrity. In contrast, perfusion with free oHSV-1 (bottom row) results in intense red fluorescence throughout the BBB region, consistent with widespread infection and potential barrier disruption. These data suggest that monocyte-mediated delivery significantly limits direct viral exposure to the BBB, although a minimal leakage or interaction cannot be completely excluded.

Migration of human primary monocytes through the BBB was evident as early as 24 h post-perfusion, with green-labeled cells detected in the bottom layer of the BBB, in the connecting channels, and in the microwells containing U87 GBM spheroids (Fig. 4B). The presence of tumor spheroids enhanced monocyte recruiting, indicating a chemotactic interplay between GBM cells, monocytes, and the BBB, possibly contributing to localized permeability increases and immune cell homing to the tumor site. By 48 h (Fig. 4A), monocytes were found adjacent to or infiltrating GBM spheroids, and red fluorescence from oHSV-1-mCherry replication became apparent. By day 5, red fluorescence spread throughout the tumor spheroids (Fig. 4B), confirming successful delivery and transmission of viral infection by monocytes. Notably, spheroids displayed compromised morphology and lost their typical round, compact structure, with detaching infected cells visible, likely because of viral cytopathic effects. These findings support the capacity of monocyte-mediated oHSV-1 delivery to reach and kill GBM cells within the BBB-on-chip model.

2.5. Human primary monocytes cross the BBB and protect oHSV-1-mCherry from antibody-mediated neutralization, enabling viral transmission to GBM tumor spheroids

Systemic delivery of free OVIs is frequently limited by neutralization from pre-existing host immunity, particularly in the case of agents derived from viruses with high human seroprevalence, such as HSV-1 [33]. Carrier cells can protect OVIs from immune surveillance and thereby enhance their therapeutic potential. To evaluate if autologous monocytes can shield oHSV-1 from antibody-mediated neutralization, we used a human hyperimmune IgG preparation that mimics the natural immune milieu by targeting a broad spectrum of human pathogens, including HSV-1. Two conditions were tested: a 1:4 dilution of hyperimmune IgG, which fully neutralized oHSV-1-mCherry in U87 GBM cells, and a 1:8 dilution, which only partially restricted viral spread without completely blocking replication (Supplementary Figure S4).

Fig. 5 summarizes the key findings obtained from GBM spheroids under both static and BBB-on-chip culture conditions. In static microwell cultures, control spheroids treated with free oHSV-1-mCherry in the absence of antibodies showed progressive infection, with red fluorescence spreading throughout the spheroid by day 7. However, in the presence of hyperimmune IgGs (1:8 dilution), viral dissemination was markedly suppressed: no red signal was detected until day 4, and only sparse fluorescence appeared by day 7 (Fig. 5A). In contrast, spheroids treated with primary human monocytes pre-loaded with oHSV-1-mCherry (labeled with CellTracker™ Green), exhibited evident viral

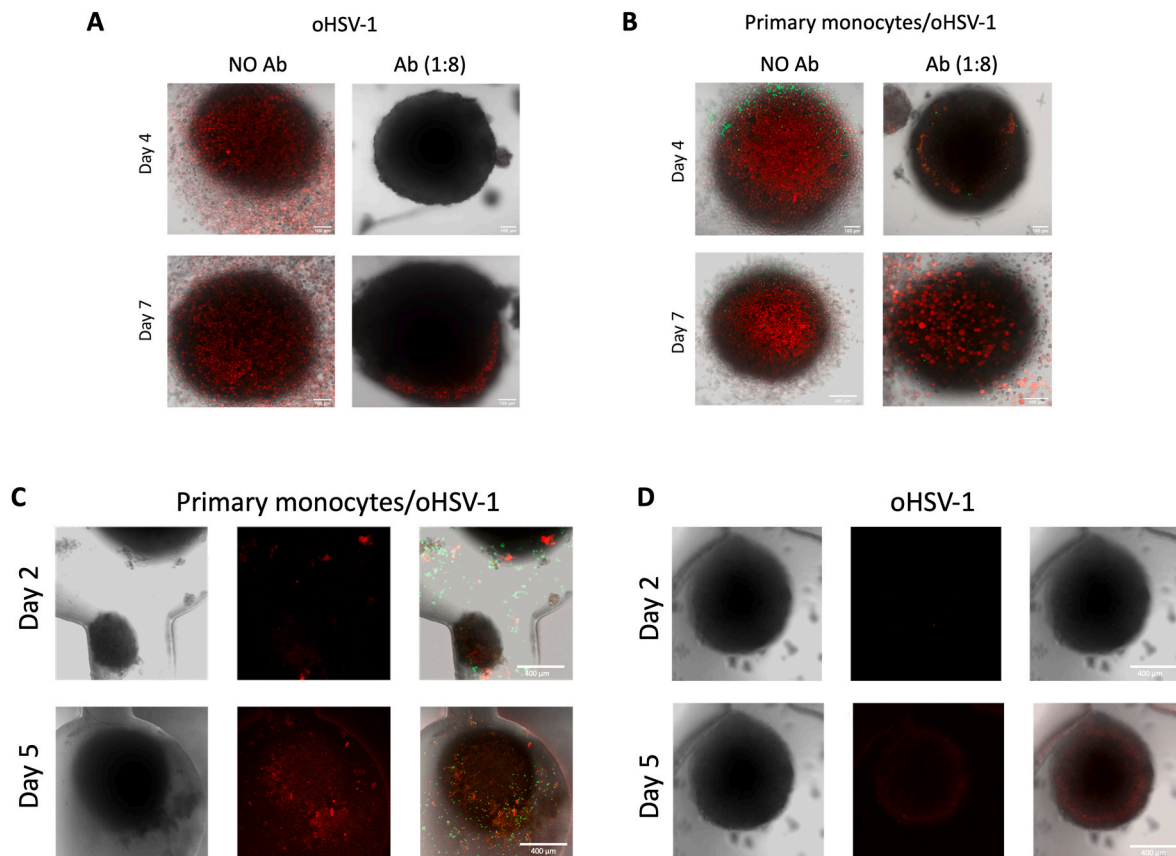


Fig. 5. Human monocytes efficiently shield their oHSV-1 cargo from neutralizing human hyperimmune gamma globulins. **A.** Time course of GBM spheroids infected with free oHSV-1 mCherry (1.5×10^3 PFU/well) in static microwells with and without human hyperimmune IgGs (1:8 dilution). Scale bars 400 and 100 μ m. **B.** Tumor spheroids treated with primary human monocytes infected with oHSV-1-mCherry (MOI = 3 PFU/cell, 5×10^3 cells/well) in static microwells with and without human hyperimmune IgGs (1:8 dilution). **C.** Primary human monocytes infected with oHSV-1 mCherry (MOI = 3 PFU/cell, 3×10^5 cells/chip) are perfused in the BBB-on-chip models in the presence of human hyperimmune IgGs (1:8 dilution) and monitored for 5 days confirming successful transmission of the infection. **D.** In a similar experimental setup, free virus (9×10^5 PFU/chip) is perfused in the BBB-on-chip in the presence of human hyperimmune IgGs (1:8 dilution) and monitored for 5 days confirming viral neutralization.

replication by day 4, regardless of antibody presence. Infection continued to expand through day 7 in both control and IgG-treated samples (Fig. 5B). These results indicate that monocytes carriers can effectively protect oHSV-1-mCherry from antibody-mediated inactivation in static conditions.

We then evaluated this mechanism in the BBB-on-chip model, in which GBM spheroids reside in microwells of the tumor compartment. Hyperimmune IgGs (1:8 dilution) were perfused alongside either free virus or oHSV-1-loaded primary human monocytes. After 48 h of perfusion, green-labeled monocytes were detected in the apical (brain-facing) compartment of the device, confirming successful transmigration across the BBB (Fig. 5C). Red fluorescence was also observed at this time point, indicating effective viral transmission to tumor cells. In contrast, chips perfused with free oHSV-1-mCherry showed no significant red signal, confirming that the virus had been neutralized by circulating IgGs (Fig. 5D).

3. Conclusion

Previous studies, including our own, have shown that monocytes are susceptible but not fully permissive to HSV-1 replication [16,34]. Nevertheless, we demonstrated in transwell-based systems that oHSV-1-infected monocytes retain their ability to migrate toward tumor cells, where viral replication is reactivated and leads to effective oncolysis. Similar results were observed *in vivo* using the chorioallantoic membrane (CAM) model [16]. In this study, we extended these findings by developing and applying a dynamic, physiologically relevant BBB-on-chip platform to investigate the interactions among monocytes, oncolytic viruses (OVs), and the blood–brain barrier (BBB). While several advanced BBB-on-chip systems have been reported [35,36], our model offers a unique balance of simplicity, functionality, and adaptability. Its streamlined design accelerates barrier maturation, while its modular structure easily integrates 3D tumor spheroids. Furthermore, the use of pump-driven perfusion enables controlled and physiologically relevant shear stress, enhancing the biological fidelity of the model. These features address key limitations of existing platforms and make our chip a versatile and practical tool for studying BBB-tumor interactions, therapeutic delivery, and barrier integrity under dynamic conditions.

Monocytes are naturally capable of crossing the BBB via both the transcellular [37] and paracellular [38] routes, guided by chemotactic signals. Although some migration occurs under physiological conditions, it is enhanced in pathological settings such as infection, inflammation, and brain tumors [39]. Several viruses, including HIV [40], Zika virus [41], and enterovirus A71 [42], have been shown to exploit infected monocytes as “Trojan horse” carriers to enter the central nervous system.

Our BBB-on-chip model confirms that primary human monocytes can traverse the BBB and deliver oHSV-1 to GBM spheroid. Within this microphysiological environment, viral replication was reactivated, resulting in effective infection and oncolysis. By demonstrating both the therapeutic potential of monocyte-based OVs delivery and the utility of a simplified yet biologically relevant BBB-on-chip platform, this work lays the groundwork for future studies aimed at refining cell-based viral therapies for GBM and other CNS malignancies. Our key findings are summarized below.

- **Directed monocyte migration:** monocytes preferentially migrate across the BBB in the presence of GBM spheroids, consistent with evidence that monocytes and tumor-associated macrophages (TAMs) are actively recruited to the TME through chemotactic cues (e.g., CD62L, CCL2, CXCL1, VEGF-A) and their receptors (e.g. CD62R, CCR2, CX3CR1, and VEGFR1) [43]. Our results confirm and expand upon a recent study showing that THP-1 monocytes migrate across an endothelial barrier only in the presence of GBM spheroids [44]. Although the brain contains its own resident phagocytes (microglia),

it has been demonstrated that a substantial proportion of TAMs in GBM arise from circulating monocytes [45]. It is therefore possible that the infiltration of oHSV-1-loaded monocytes into GBM spheroids observed in our experiments correlates with their differentiation into TAM-like cells, a hypothesis that warrants further investigation.

- **Tumor-triggered viral replication:** infected monocytes do not release the virus while in circulation, as demonstrated by the reduced infection of BBB-resident cells compared to free oHSV-1. Upon reaching GBM spheroids, however, viral replication is reactivated, leading to tumor cell infection and death. These findings support the feasibility of using monocytes as safe and efficient viral carriers. Notably, monocyte differentiation triggered by tumor contact may enhance HSV-1 permissiveness, as suggested by previous reports [34, 46]. Our model provides a suitable platform to further explore this hypothesis and to investigate the molecular mechanisms behind the recruitment and activation of oHSV-1 infected monocytes.
- **Immune shielding:** oHSV-1 carried by monocytes is effectively protected from neutralizing antibodies. Even in the presence of hyperimmune IgGs, viral delivery to and infection of GBM spheroids remain robust, unlike free virus, which is rapidly neutralized.
- **Localized infection control:** monocyte-mediated delivery restricts viral infection to the tumor site, minimizing off-target infection of other cell populations, including BBB-resident cells.

Several strategies have been proposed to achieve systemic delivery of OVs using non-cellular nanocarriers. For example, biocompatible magnetic nanoparticles derived from magnetotactic bacteria have been explored for oHSV-1 delivery, showing promising results but with important limitations, such as the need to eliminate toxic bacterial components and the variability of nanoparticle uptake across cell lines [47]. Various formulations for nucleic acid delivery as gene therapies have also been developed [48], however, in GBM these approaches still require intracranial or intrathecal administration, highlighting the challenge posed by the BBB [49].

Oncolytic virotherapy differs fundamentally from other therapeutic modalities, as the “drug” (the OV) can actively replicate and propagate within infected cells. In this context, using monocytes as cellular carriers offers significant advantages over non-living vehicles, as they can actively migrate toward tumor sites, including small or undetectable micrometastases [50]. While artificial targeting using magnetic guidance, as in Howard et al., [47] is feasible, it requires site-specific stimulation and ultimately behaves similarly to localized intratumoral injection. By contrast, autologous monocytes can be readily obtained from peripheral blood and infected *ex vivo* without extensive manipulation. In the future, an off-the-shelf approach could be envisioned using immune-evasive induced pluripotent stem cells (iPSCs) differentiated into monocytes [51,52].

Overall, our results support the use of autologous monocytes as a “Trojan horse” strategy for the systemic delivery of OVs to GBM. This approach offers a minimally invasive, immune-evasive, and targeted therapeutic alternative to intracranial injection, with significant implications for patient compliance and clinical translation. Future studies will focus on further optimizing this strategy and assessing its safety and therapeutic efficacy in preclinical and clinical settings.

4. Experimental section

BBB-on-chip design and fabrication: The geometry of the BBB-on-chip was designed using AutoCAD® software, and the master mold was fabricated on a silicon wafer using standard photolithography [33]. The microfluidic device was replica molded in polydimethylsiloxane (PDMS; Sylgard 184; Dow Corning, Midland, MI, USA) using soft lithography techniques [53]. Briefly, PDMS pre-polymer (10:1 elastomer base to curing agent, wt/wt) was degassed and poured over the SU-8 (Microchem, Newton, MA, USA) patterned wafer to imprint the apical and basolateral geometries. After curing at 80 °C, for 1 h, the inlets and

outlets were created using a 1 mm diameter biopsy punch. A transparent polyester membrane (PETE, 3 μm pore size, 12 μm thickness, Sterlitech Corp, Kent, WA, USA) was sandwiched and bonded between the apical and the basolateral PDMS layers using a plasma cleaner (Harrick Plasma, Ithaca, NY, USA). The assembled BBB-on-chip devices were bound to glass coverslips via further plasma treatment and sterilized with 70 % ethanol followed by UV exposure for 60 min.

BBB-on-chip cells seeding and culturing: Human umbilical vein endothelial cells (HUVECs), brain vascular pericytes (hBVPs), and immortalized astrocytes (hAs) were obtained from Innoprot (Derio, Spain). HUVECs were expanded in fibronectin-coated (FN, Innoprot, 1 mg/ml) 75 cm^2 flasks using Endothelial Basal Medium (P60104, Innoprot) supplemented with 5 % fetal bovine serum (FBS, Innoprot), 1 % penicillin-streptomycin (P/S, Innoprot), and 1 % endothelial cell growth supplement (ECGS, Innoprot). hBVPs and hAs were cultured in poly-L-lysine-coated (PLL, Innoprot, 1 mg/ml) 25 cm^2 flasks using Pericyte and Astrocyte Basal Medium, respectively, supplemented with 2 % FBS, 1 % growth supplement, and 1 % P/S solution. For BBB-on-chip seeding, the PETE membrane was coated for 24 h with FN (blood side) and PLL (brain side), followed by three Phosphate Buffer Saline (PBS, Sial s.r.l., Rome, Italy) washes. hAs and hBVPs were seeded on the brain side at densities of 5×10^5 and 1×10^5 cells, respectively. After 6 h of inverted incubation to favor cell adhesion to the PETE membrane, devices were placed upright and incubated for 24 h with medium changes every 8 h (medium 1:1 mix of hAs and hBVP media). HUVECs were seeded at 6×10^6 cells/mL in the vascular channel (blood side) and incubated for 4 h. Devices were then perfused at 30 $\mu\text{L}/\text{min}$ using tubing connected to inlet/outlet ports. The perfusion medium was composed of 75 % HUVEC medium and 25 % (1:1) hAs/hBVP media (please see [Supplementary Figure S5](#) for optimization details). Devices were cultured for 7 days to ensure the correct formation and maturation of the BBB before experimentation.

TEER measurements: TEER values were monitored over 7 days using a Millicell-ERS2 volt-ohm meter (Millipore, Merck, Rahaway, NJ, USA) with STX01 electrodes. TEER values correlate with BBB formation and maturation. Measurements were recorded by placing electrodes at the blood and brain sides of the PETE membrane. Devices without served as blanks. TEER was calculated using the following [formula \(1\)](#).

$$TEER = (R - R_{\text{blank}}) * A \quad (1)$$

where A is the membrane area, R is the measured resistance in the seeded BBB-on-chip device, and R_{blank} is the resistance in the blank device.

Characterization of BBB permeability: Permeability was assessed using 40, 70, and 150 kDa Fluorescein isothiocyanate isomer-dextran (FITC-dextran, 0.5 mg/mL). Three experimental groups were used: no cells, endothelial-only, and complete BBB (triculture). On day 7, the devices were perfused with FITC-dextran through the blood channel at 5 $\mu\text{L}/\text{min}$ and imaged at three regions of interest (ROIs) on the brain side in correspondence of the three microwells. Permeability is determined using a standard reference method, and the Apparent permeability (P_{app}) and BBB-specific permeability (P_{BBB}) were calculated using equations (2) and (3) [54].

$$P_{\text{app}} = \frac{C_{(t)} V}{C_0 A \Delta T} \quad (2)$$

$$\frac{1}{P_{\text{BBB}}} = \frac{1}{P_{\text{app}}} - \frac{1}{P_0} \quad (3)$$

where $C_{(t)}$ is dextran concentration in the brain side, V is volume, C_0 is blood-side concentration, A is surface area, ΔT is the assay time, and P_0 is the permeability of the blank device.

Shear stress calculation and modeling: Computational Fluid Dynamics (CFD) simulations were conducted using COMSOL Multiphysics 6.1 to model shear stress in the blood-side channel. The simulation used a

laminar flow model, incorporating geometry, meshing, and inflow boundary condition sweeps to achieve the desired shear stress level. The working fluid was modeled as incompressible Newtonian mimicking culture media [55,56]. Calculated Reynolds numbers remained below 2000, confirming laminar flow conditions.

Immunofluorescence staining (IF): Cells within the BBB-on-chip were analyzed via IF for zonula occludens protein-1 (ZO-1), CD31, glial fibrillary acidic protein (GFAP) on day 7 of culture. For staining, cells were fixed on-chip using 4 % paraformaldehyde (PFA, Sigma-Aldrich, Merck) in PBS, followed by permeabilization with 0.1 % Triton X-100 (Sigma-Aldrich, Merck). Samples were then blocked at room temperature for 1 h using PBS containing 5 % bovine serum albumin (BSA, Sigma-Aldrich, Merck) and 0.1 % Triton X-100. Subsequently, chips were incubated overnight at 4 $^{\circ}\text{C}$ with primary antibodies diluted in PBS containing 5 % BSA and 0.1 % Triton X-100: mouse anti-CD31 (1:200, Proteintech Group, Inc, Rosemont, IL, USA, 66065-2-Ig), mouse anti-ZO-1 (1:50, Proteintech, 66452-1-Ig), and rabbit anti-GFAP (1:200, Proteintech, 60190-1-Ig). After washing, samples were incubated for 1 h at room temperature with Coralite488-conjugated goat anti-mouse (1:800, Proteintech, SA00013-1) and Coralite647-conjugated goat anti-rabbit (1:800, Proteintech, SA00014-9) secondary antibodies in PBS with 5 % BSA and 0.1 % Triton-X100. Following additional washes, nuclei were counterstained with DAPI (0.1 $\mu\text{g}/\text{mL}$, Sigma-Aldrich, MBD0020) in PBS for 10 min. Finally, samples were mounted using 80 % glycerol (Sigma-Aldrich, Merck) in Milli-Q water. Imaging is performed using a confocal microscope (LSM 700, Zeiss, Milan, Italy).

Spheroid formation and characterization: U87 glioblastoma cells (U-87 MG, ATCC HTB-14TM) were maintained as monolayers in DMEM high glucose (Sial s.r.l.) supplemented with 10 % FBS (Thermo Fisher Scientific, Waltham, MA, USA), 1 % MEM non-essential amino acids (NEAA, Thermo Fisher Scientific) and 1 % P/S (Sial s.r.l.), under standard cell conditions (37 $^{\circ}\text{C}$, 5 % CO_2 , humidified atmosphere). Media were refreshed every 2–3 days. Spheroids were generated from trypsinized monolayer cells, as previously described [57]. Briefly, 200 μL of cell suspension containing 2×10^3 cells were seeded into each well of an Ultra-Low Attachment (ULA) 96-well round bottom plate (Corning[®], Thermo Fisher Scientific) and centrifuged at 130 g for 10 min to promote aggregation. Spheroids were cultured for 7 days, with medium replenishment on day 4. Spheroid morphology and growth were monitored via brightfield imaging (Evos Imaging System, Thermo Fisher). Morphometric parameters, including size, solidity, and sphericity index (SI), were analyzed using AnaSP, an open-source software [58]. On day 7, viability was assessed using a Live/Dead assay with Calcein-AM (1 $\mu\text{g}/\text{mL}$, Sigma-Aldrich, 17783), Hoechst 33342 (2 $\mu\text{g}/\text{mL}$, Sigma-Aldrich, 14533) and Propidium Iodide (50 $\mu\text{g}/\text{mL}$, Sigma-Aldrich, P4864) in PBS. After replacing the culture medium with 100 μL of staining solution, spheroids were incubated for 30 min at room temperature in the dark and then imaged using a fluorescence microscope (Axio Imager M1, Zeiss). For cytoskeletal labeling, spheroids were fixed on day 7 with 4 % PFA, permeabilized using 0.1 % Triton X-100, and incubated with CoraLite594-conjugated Coralite[®]594-Phalloidin (1:400, Proteintech, PF000003) in PBS for 1 h at room temperature. Samples were washed, stained with DAPI (1:100) in PBS for 20 min, washed again, and finally imaged using a Zeiss LSM 700 confocal microscope.

oHSV-1-mCherry production: oHSV-1-mCherry ($\Delta\gamma34.5/\Delta\text{Us}12/\text{miRNA}124/\text{mCherry-oHSV-1}$) is an engineered oncolytic herpes simplex virus type 1 (oHSV-1) with a genomic backbone similar to the clinically approved T-VEC (talimogene laherparepvec). This construct contains deletions of the $\gamma34.5$ and $\text{Us}12$ genes, which contribute to viral neuroattenuation, but lacks the two copies of the human GM-CSF gene present in T-VEC. Additionally, it bears an mCherry expression cassette inserted into the UL55-UL56 intergenic region. Further neuroattenuation is achieved by incorporating miR-124 target sequences downstream of the essential gene $\text{UL}29$, to further impair viral replication in mature neurons where miR-124 is expressed. This virus was

obtained via bacterial artificial chromosome (BAC) mutagenesis, following previously described protocols [59]. The starting material is a BAC containing the full-length genome of HSV-1 strain 17⁺, modified to include γ 34.5 deletions and an eukaryotic cassette encoding for firefly luciferase within the UL55-UL56 intergenic region. This BAC was kindly provided by Beate Sodeik (Hannover Medical School, Germany). To reconstitute infectious virus, the modified BAC was transfected into 293T cells using Lipofectamine 2000TM (InvitrogenTM, Thermo Fisher Scientific). Viral stocks were then amplified in green monkey kidney Vero cells and quantified via plaque titration assay on Vero cells, as previously reported [60].

Static infection of U87-MG spheroids with oHSV-1-mCherry transported by THP-1 cells: After 7 days of maturation, U87-MG spheroids were inoculated with the oncolytic herpes simplex virus type 1 (oHSV-1)-mCherry at a multiplicity of infection (MOI) of 3 plaque forming units (PFU)/cell. THP-1 cells (ATCC TIB-202TM) were cultured in Roswell Park Memorial Institute (RPMI, Gibco) medium supplemented with 10 % FBS (Thermo Fisher Scientific) and 1 % P/S, under standard cell culture conditions. Prior to infection, THP-1 cells were labeled with CellTrackerTM Green (C2925, InvitrogenTM, Thermo Fisher Scientific) by incubation in serum-free RPMI containing the dye (0.5 μ L/mL) for 20 min at 37 °C. Following labeling, cells were centrifuged (at 300 g, 5 min), washed twice with PBS, and resuspended in serum-free RPMI. Cells were then infected with oHSV-1-mCherry by incubation for 60 min at 37 °C. Post-infection, cells were pelleted, washed three times with PBS to remove extracellular virions and resuspended in DMEM supplemented with 10 % FBS. Approximately 500 infected THP-1 cells were added to each spheroid-containing well. Viral spread was monitored over time using confocal microscopy by tracking mCherry fluorescence. In parallel, the metabolic activity of the spheroids was assessed via an MTT assay (Sigma-Aldrich, Merck), serving as a proxy for cell viability and proliferation. Briefly, at selected time points, individual spheroids were transferred to flat bottom 96-well plates containing 100 μ L/well of fresh medium and 50 μ L/well of MTT solution (5 mg/mL PBS). After a 4-h incubation at 37 °C in the dark, the resulting formazan crystals were solubilized with 50 μ L/well of DMSO. Absorbance was measured at 560 nm using a Spark[®] Multimode Microplate Reader (Tecan Group Ltd., Männedorf, Switzerland), and viability was relative to untreated control spheroids.

Perfusion of THP-1 cells infected with oHSV-1-mCherry in the BBB-on-chip: Upon full maturation of the BBB structure within the microfluidic devices, at day 7 U87-MG spheroids were transferred from ULA plates into the microwells of the BBB-on-chip (one spheroid per microwell, three per device). THP-1 cells were labeled with CellTrackerTM Green and infected with oHSV-1-mCherry at a MOI of 3 PFU/cell, as previously described. After infection, cells were centrifuged (1000 g, 5 min), washed three times with PBS, and resuspended in 2 mL of DMEM supplemented with 10 % FBS, yielding a final concentration of 2.5×10^5 cells per mL. Infected THP-1 cells were perfused into the blood-side inlet of the microfluidic device using 5 mL Luer lock syringes (BD PlastiPakTM, Sial s.r.l.) at a flow rate of 5 μ L/min. Control conditions include perfusion of: *i.* non-infected THP-1 cells ($\sim 5 \times 10^5$ per device) labeled only with CellTrackerTM Green, and *ii.* free oHSV-1-mCherry, added directly to the perfusion medium in equivalent viral doses to those used for THP-1 infection.

Primary human monocytes isolation: Primary human monocytes were isolated from buffy coats derived from the peripheral blood of healthy donors, provided by the Transfusion Center of the University Hospital of Padua. No prior approval from an ethical committee is required, as samples are obtained as byproducts of routine blood draws without any additional intervention or burden to the donor and all samples are fully anonymized and handled in compliance with relevant data protection and bioethics regulations. All donors were screened to exclude HIV, HBV, HCV, and Treponema pallidum infections. Peripheral Blood Mononuclear Cells (PBMCs) were first separated by density gradient centrifugation using Ficoll-Paque[®] Plus (GE17-1440-03, Sigma-Aldrich,

Merck), following the manufacturer's protocol. Briefly, the buffy coat was gently mixed by inversion (6–8 times), then diluted 1:1 with serum-free RPMI. A layer of Ficoll was carefully added to the bottom of a Falcon tube, and the diluted blood was layered on top without disturbing the gradient. The tubes were then centrifuged at 1000 g for 20 min. The resulting PBMC layer was carefully collected and transferred to a fresh tube [61]. Next, cells underwent three washes with PBS, each followed by centrifugation at 1000g for 8 min. A final wash at 800 g for 10 min removed residual platelets. Monocytes were then positively selected using the EasySepTM Human CD14 Positive Selection Kit II (StemcellTM Technologies, Vancouver, Canada), according to the manufacturer's instructions.

Flow cytometry analysis for human primary monocytes: Following isolation, human primary monocytes were counted using a hemocytometer or an automated cell counter. To assess purity, 1×10^6 cells were resuspended in PBS and incubated with a fluorophore-conjugated anti-CD14 antibody (CD14V450, Becton Dickinson, Milan, Italy) for 30 min at 4 °C in the dark. After incubation, cells were washed and resuspended in PBS. Samples were analyzed using a flow cytometer (FACS Canto II, Becton Dickinson) with gating applied to viable single cells. Monocyte purity was determined based on the percentage of CD14⁺ cells, with a threshold of ≥ 80 % indicating successful isolation.

Static and BBB-on-chip infection of U87-GBM spheroids with oHSV-1-mCherry transported by primary monocytes: The static infection of U87-GBM spheroids with human primary monocytes was performed according to the protocols described in the previous sections. Human primary monocytes, isolated from buffy coats, were infected with oHSV-1-mCherry for 1 h at 37 °C. For consistency, we decided to adopt the same 3 PFU/cell MOI used for THP-1 cells. After infection, cells were labeled with CellTrackerTM Green (diluted in serum-free RPMI) by incubating for 20 min at 37 °C. Monocytes were then pelleted, resuspended in DMEM supplemented with 10 % FBS, and added to preformed U87-MG tumor spheroids at a concentration of 5×10^3 cells per spheroid. For BBB-on-chip experiments, primary human monocytes were stained with CellTrackerTM Green and infected with oHSV-1-mCherry at an MOI of 3 PFU/cell, as described above. Following infection, monocytes were resuspended in 2 mL of DMEM supplemented with 10 % FBS to achieve a final concentration of 3×10^5 cells/mL. This suspension was loaded into 5 mL Luer-lock syringes and perfused through the blood-side inlet of the BBB-on-chip device at a constant flow rate of 5 μ L/min. Control conditions included: *i.* non-infected primary monocytes labeled only with CellTrackerTM Green (3×10^5 cells per device), and *ii.* free oHSV-1-mCherry, both following the same perfusion protocol.

Experiments on antibody neutralization in static and BBB-on-chip conditions using infected primary monocytes: Following infection, human primary monocytes stained with CellTrackerTM Green were resuspended in DMEM supplemented with 10 % FBS and a 1:8 dilution of Human Gamma Globulin Control antibodies (IgG, Invitrogen, Thermo Fisher Scientific). A total of 5×10^3 monocytes were added to each U87 GBM spheroid, which was resuspended in 100 μ L of DMEM containing 10 % FBS and 1:8 IgG. In parallel, U87-MG spheroids were directly infected with free oHSV-1-mCherry, using the same viral load used for infecting monocytes, in the presence of 1:8 diluted antibodies. Viral replication and spread within the tumor spheroids were monitored by confocal microscopy. Control spheroids, treated with either oHSV-1-mCherry-infected primary monocytes or free virus, were maintained in DMEM with 10 % FBS in the absence of immunoglobulins. For BBB-on-chip studies, infected monocytes were resuspended in 2 mL of DMEM containing 10 % FBS and a 1:8 dilution of human IgG. The cell suspension was then perfused into the device through the blood-side inlet. Spheroids within the BBB-on-chip were monitored over several days using confocal microscopy to assess differences in viral propagation in the presence of neutralizing antibodies, based on the delivery strategy of the oncolytic virus.

Statistical Analysis: Graphs were compiled using OriginPro[®] software, and statistical analyses were performed using GraphPad Prism. All

graphical data represent the mean \pm standard error of the mean (SEM) from at least three independent experiments. Comparisons between multiple groups were conducted using one-way ANOVA, while comparisons between two groups were performed using the Student's t-test. Statistical significance is indicated by asterisks, denoting differences between treated and control groups unless otherwise specified. * $p < 0.05$, ** $p < 0.01$, *** $p < 0.001$, **** $p < 0.0001$.

CRedit authorship contribution statement

Sara Micheli: Writing – review & editing, Writing – original draft, Visualization, Methodology, Investigation, Formal analysis, Data curation, Conceptualization. **Alberto Reale:** Writing – review & editing, Methodology, Investigation, Data curation, Conceptualization. **Alessandra Rossetto:** Writing – review & editing, Methodology, Investigation, Formal analysis. **Cristina Parolin:** Writing – review & editing, Methodology, Funding acquisition, Conceptualization. **Fabio Mammano:** Writing – review & editing, Funding acquisition, Conceptualization. **Arianna Calistri:** Writing – review & editing, Project administration, Methodology, Funding acquisition, Data curation, Conceptualization. **Elisa Cimetta:** Writing – review & editing, Supervision, Project administration, Methodology, Funding acquisition, Data curation, Conceptualization.

Conflict of interest

The authors declare no conflict of interest.

Declaration of competing interest

The authors declare that they have no known competing financial interests or personal relationships that could have appeared to influence the work reported in this paper.

Acknowledgements

This research project has received funding from the European Commission, ARACHNID project (ERC-2023-POC, id: 55008, CIME_UER124_01) to E.C. and INFRAPLUS (Proposal number: 101131669, Proposal title: Enhancing and Evolving INFRAFRONTIER Disease Modelling Capacity to Enable Breakthrough Research) to F.M.; Fondazione Giovanni Celegghin Contro I Tumori Cerebrali to A.C.; Associazione Italiana per la Ricerca sul Cancro (AIRC IG 27797) to F.M.; Italian Ministry of Research and University (PRIN2022A5YWJJ) to F.M.; University of Padova (PARO_FINA20_01) to C.P.

Appendix A. Supplementary data

Supplementary data to this article can be found online at <https://doi.org/10.1016/j.mtbio.2025.102458>.

Data availability

All original data are available at: <https://researchdata.cab.unipd.it/id/eprint/1544>

References

- [1] B. Obermeier, R. Daneman, R.M. Ransohoff, Development, maintenance and disruption of the blood-brain barrier, *Nat. Med.* 19 (2013) 1584, <https://doi.org/10.1016/j.mtbio.2025.101652>.
- [2] R. Pandit, L. Chen, J. Götz, The blood-brain barrier: physiology and strategies for drug delivery, *Adv. Drug Deliv. Rev.* 1 (2020) 165–166, <https://doi.org/10.1016/j.addr.2019.11.009>.
- [3] K.H. Narsinh, E. Perez, A.F. Haddad, J.S. Young, L. Savastano, J.E. Villanueva-Meyer, E. Winkler, J. de Groot, Strategies to improve drug delivery across the blood–brain barrier for glioblastoma, *Curr. Neurol. Neurosci. Rep.* 24 (2024) 123, <https://doi.org/10.1007/s11910-024-01338-x>.
- [4] H.-G. Wirsching, E. Galanis, M. Weller, Glioblastoma, *Handb. Clin. Neurol.* 134 (2016) 381, <https://doi.org/10.1016/B978-0-12-802997-8.00023-2>.
- [5] T. Tykocki, M. Eltayeb, Ten-year survival in glioblastoma. A systematic review, *J. Clin. Neurosci. Off. J. Neurosurg. Soc. Australas.* 54 (2018) 7, <https://doi.org/10.1016/j.jocn.2018.05.002>.
- [6] R. Medikonda, G. Dunn, M. Rahman, P. Fecci, M. Lim, A review of glioblastoma immunotherapy, *J. Neuro Oncol.* 151 (2021) 41, <https://doi.org/10.1007/s11060-020-03448-1>.
- [7] C.E. Brown, A. Rodriguez, et al., Off-the-shelf, steroid-resistant, IL13R α 2-specific CAR T cells for treatment of glioblastoma, *Neuro Oncol.* 24 (2022) 1318, <https://doi.org/10.1093/neuonc/noac024>.
- [8] D.M. O'Rourke, M.P. Nasrallah, et al., A single dose of peripherally infused EGFRvIII-directed CAR T cells mediates antigen loss and induces adaptive resistance in patients with recurrent glioblastoma, *Sci. Transl. Med.* 19 (9) (2017) eaaa0984, <https://doi.org/10.1126/scitranslmed.aaa0984>, 399.
- [9] B.D. Choi, E.R. Gerstner, M.J. Frigault, M.B. Leick, C.W. Mount, L. Balaj, S. Nikiforow, B.S. Carter, W.T. Curry, K. Gallagher, M. V Maus, Intraventricular CARv3-TEAM-E T cells in recurrent glioblastoma, *N. Engl. J. Med.* 390 (2024) 1290, <https://doi.org/10.1056/NEJMoa2314390>.
- [10] S.J. Russell, K.-W. Peng, J.C. Bell, Oncolytic virotherapy, *Nat. Biotechnol.* 30 (2012) 658, <https://doi.org/10.1038/nbt.2287>.
- [11] A. Reale, A. Vitiello, V. Conciatori, C. Parolin, A. Calistri, G. Palù, Perspectives on immunotherapy via oncolytic viruses, *Infect. Agent. Cancer* 14 (2019) 5, <https://doi.org/10.1186/s13027-018-0218-1>.
- [12] R.M. Conry, B. Westbrook, S. McKee, T.G. Norwood, Talimogene laherparepvec: first in class oncolytic virotherapy, *Hum. Vaccin. Immunother.* 14 (2018) 839, <https://doi.org/10.1080/21645515.2017.1412896>.
- [13] T. Todo, H. Ito, Y. Ino, H. Ohtsu, Y. Ota, J. Shibahara, M. Tanaka, Intratumoral oncolytic herpes virus G47 Δ for residual or recurrent glioblastoma: a phase 2 trial, *Nat. Med.* 28 (2022) 1630, <https://doi.org/10.1038/s41591-022-01897-x>.
- [14] R.A. Ageeb, M. Harfouche, H. Chemaitelly, L.J. Abu-Raddad, Epidemiology of herpes simplex virus type 1 in the United States: systematic review, meta-analyses, and meta-regressions, *iScience* 27 (2024) 110652, <https://doi.org/10.1016/j.isci.2024.110652>.
- [15] A. Hadrys, A. Sochanik, G. McFadden, J. Jazowiecka-Rakus, Mesenchymal stem cells as carriers for systemic delivery of oncolytic viruses, *Eur. J. Pharmacol.* 874 (2020) 172991, <https://doi.org/10.1016/j.ejphar.2020.172991>.
- [16] A. Reale, L. Krutke, M. Cadamuro, A. Vitiello, J. von Einem, S. Kochanek, G. Palù, C. Parolin, A. Calistri, Human monocytes are suitable carriers for the delivery of oncolytic Herpes simplex virus type 1 in vitro and in a chicken embryo chorioallantoic membrane model of cancer, *Int. J. Mol. Sci.* 24 (2023) 9255, <https://doi.org/10.3390/ijms24119255>.
- [17] M.A. Deli, G. Porkoláb, A. Kincses, M. Mészáros, A. Szecskó, A.E. Kocsis, J.P. Vigh, S. Valkai, S. Veszelka, F.R. Walter, A. Dér, Lab-on-a-chip models of the blood–brain barrier: evolution, problems, perspectives, *Lab Chip* 24 (2024) 1030, <https://doi.org/10.1039/D3LC00996C>.
- [18] S. Reshma, K.B. Megha, S. Amir, S. Rukhiya, P. V Mohanan, Blood brain barrier-on-a-chip to model neurological diseases, *J. Drug Deliv. Sci. Technol.* 80 (2023) 104174, <https://doi.org/10.1016/j.jddst.2023.104174>.
- [19] L. Cucullo, M. Hossain, V. Puvanna, N. Marchi, D. Janigro, The role of shear stress in Blood-Brain Barrier endothelial physiology, *BMC Neurosci.* 12 (2011) 40, <https://doi.org/10.1186/1471-2202-12-40>.
- [20] E. Jagtiani, M. Yeolekar, S. Naik, V. Patravale, In vitro blood brain barrier models: an overview, *J. Control. Release* 343 (2022) 13, <https://doi.org/10.1016/j.jconrel.2022.01.011>.
- [21] C.E. Stăicu, F. Jipa, E. Axente, M. Radu, B.M. Radu, F. Sima, Lab-on-a-Chip platforms as tools for drug screening in neuropathologies associated with blood–brain barrier alterations, *Biomolecules* 11 (6) (2021) 916, <https://doi.org/10.3390/biom11060916>.
- [22] W. Bi, S. Cai, T. Lei, L. Wang, Implementation of blood-brain barrier on microfluidic chip: recent advance and future prospects, *Ageing Res. Rev.* 87 (2023) 101921, <https://doi.org/10.1016/j.arr.2023.101921>.
- [23] L.M. Griep, F. Wolbers, B. de Wagenaar, P.M. ter Braak, B.B. Wexler, I.A. Romero, P.O. Couraud, I. Vermes, A.D. van der Meer, A. van den Berg, BBB on chip: microfluidic platform to mechanically and biochemically modulate blood-brain barrier function, *Biomed. Microdevices* 15 (2023) 145–150, <https://doi.org/10.1007/s10544-012-9699-7>.
- [24] J. Banerjee, Y. Shi, H.S. Azevedo, In vitro blood-brain barrier models for drug research: State-of-the-art and new perspectives on reconstituting these models on artificial basement membrane platforms, *Drug Discov. Today* 21 (2016) 1367–1386, <https://doi.org/10.1016/j.drudis.2016.05.020>.
- [25] T.G. Schreiner, I. Creangă-Murariu, B.I. Tamba, N. Lucanu, B.O. Popescu, In vitro modeling of the blood-brain barrier for the study of physiological conditions and Alzheimer's disease, *Biomolecules* 12 (8) (2022) 1136, <https://doi.org/10.3390/biom12081136>.
- [26] P.S. Steeg, The blood-tumour barrier in cancer biology and therapy, *Nat. Rev. Clin. Oncol.* 18 (11) (2021) 696–714, <https://doi.org/10.1038/s41571-021-00529-6>.
- [27] P. Solar, M. Hendrych, M. Barak, H. Valekova, M. Hermanova, R. Jancalek, Blood-Brain barrier alterations and edema formation in different brain mass lesions, *Front. Cell. Neurosci.* 16 (2022) 922181, <https://doi.org/10.3389/fncel.2022.922181>.
- [28] C.D. Arvanitis, G.B. Ferraro, R.K. Jain, The blood-brain barrier and blood-tumour barrier in brain tumours and metastases, *Nat. Rev. Cancer* 20 (2020) 26–41, <https://doi.org/10.1038/s41568-019-0205-x>.

- [29] L. Zhang, A. Dimberg, J. Rasouli, Editorial: the blood-brain barrier in brain tumors: molecular mechanisms and therapeutic strategies, *Front. Neurol.* 14 (2023) 1225594, <https://doi.org/10.3389/fneur.2023.1225594>.
- [30] A. Kamiya, R. Bukhari, T. Togawa, Adaptive regulation of wall shear stress optimizing vascular tree function, *Bull. Math. Biol.* 46 (1984) 127–137, <https://doi.org/10.1007/BF02463726>.
- [31] C.S. Lee, K.W. Leong, Advances in microphysiological blood-brain barrier (BBB) models towards drug delivery, *Curr. Opin. Biotechnol.* 66 (2020) 78–87, <https://doi.org/10.1016/j.copbio.2020.06.009>.
- [32] M. Ohbuchi, M. Shibuta, K. Tetsuka, H. Sasaki-Iwaoka, M. Oishi, F. Shimizu, Y. Nagasaka, Modeling of blood-brain barrier (BBB) dysfunction and immune cell migration using Human BBB-on-a-Chip for drug discovery research, *Int. J. Mol. Sci.* 25 (2024) 6496, <https://doi.org/10.1093/ijms25126496>.
- [33] H. Bradley, L.E. Markowitz, T. Gibson, G.M. McQuillan, Seroprevalence of herpes simplex virus types 1 and 2—United States, 1999–2010, *J. Infect. Dis.* 209 (3) (2014) 325–333, <https://doi.org/10.1093/infdis/jit458>.
- [34] K. Linnavuori, T. Hovi, Herpes simplex virus infection in human monocyte cultures: dose-dependent inhibition of monocyte differentiation resulting in abortive infection, *J. Gen. Virol.* 52 (1981) 381–385, <https://doi.org/10.1099/0022-1317-52-2-381>.
- [35] M. Li, M. Zhu, R. Huang, K. Wang, Z. Zeng, L. Xiao, Y. Lin, D. Liu, Blood-brain barrier microfluidic chips and their applications, *Organs-on-a-Chip* 5 (2023) 2666, <https://doi.org/10.1016/j.ooc.2023.100027>, 1020.
- [36] C. Hajal, G.S. Offeddu, Y. Shin, S. Zhang, O. Morozova, D. Hickman, C.G. Knutson, R.D. Kamm, Engineered human blood-brain barrier microfluidic model for vascular permeability analyses, *Nat. Protoc.* 17 (1) (2022) 95–128, <https://doi.org/10.1038/s41596-021-00635-w>.
- [37] H. Wolburg, K. Wolburg-Buchholz, B. Engelhardt, Diapedesis of mononuclear cells across cerebral venules during experimental autoimmune encephalomyelitis leaves tight junctions intact, *Acta Neuropathol.* 109 (2005) 181–190, <https://doi.org/10.1007/s00401-004-0928-x>.
- [38] R. Séguin, K. Biernacki, R.L. Rotondo, A. Prat, J.P. Antel, Regulation and functional effects of monocyte migration across human brain-derived endothelial cells, *J. Neuropathol. Exp. Neurol.* 62 (4) (2003) 412–419, <https://doi.org/10.1093/jnen/62.4.412>.
- [39] L. Amann, T. Masuda, M. Prinz, Mechanisms of myeloid cell entry to the healthy and diseased central nervous system, *Nat. Immunol.* 24 (3) (2023) 393–407, <https://doi.org/10.1038/s41590-022-01415-8>.
- [40] D.W. Williams, T.M. Calderon, L. Lopez, L. Carvallo-Torres, P.J. Gaskill, E. A. Eugenin, S. Morgello, J.W. Berman, Mechanisms of HIV entry into the CNS: increased sensitivity of HIV infected CD14+CD16+ monocytes to CCL2 and key roles of CCR2, JAM-A, and ALCAM in diapedesis, *PLoS One* 8 (7) (2013) e69270, <https://doi.org/10.1371/journal.pone.0069270>.
- [41] G.C. de Carvalho, M.-Y. Borget, S. Bernier, D. Garneau, A.J. da Silva Duarte, N. Dumais, RAGE and CCR7 mediate the transmigration of zika-infected monocytes through the blood-brain barrier, *Immunobiology* 224 (6) (2019) 792–803, <https://doi.org/10.1016/j.imbio.2019.08.007>.
- [42] L. Gaume, H. Chabrolles, M. Bissex, I. Lopez-Coqueiro, L. Dehouck, A. Mirand, C. Henquell, F. Gosselet, C. Archimbaud, J.-L. Bailly, Enterovirus A71 crosses a human blood-brain barrier model through infected immune cells, *Microbiol. Spectr.* 12 (2024) e0069024.
- [43] M.D. Caverzán, L. Beaugé, P.M. Oliveda, B. Cesca González, E.M. Bühler, L. E. Ibarra, *Brain Sci.* 13 (2023), <https://doi.org/10.3390/brainsci13040542>, 10.1128/spectrum.00690-24.
- [44] M.K. Marway, D. Bhagentsang, C. Venugopal, S.K. Singh, R.G. Wylie, B. Zhang, Crossing barriers: in vitro cancer model for studying monocyte migration across endothelial barriers, *ACS Biomater. Sci. Eng.* (2025), <https://doi.org/10.1021/acsbomaterials.5c00783>.
- [45] C. Xu, M. Xiao, X. Li, L. Xin, J. Song, Q. Zhan, C. Wang, Q. Zhang, X. Yuan, Y. Tan, C. Fang, Origin, activation, and targeted therapy of glioma-associated macrophages, *Front. Immunol.* 6 (13) (2022) 974996, <https://doi.org/10.3389/fimmu.2022.974996>.
- [46] K. Linnavuori, T. Hovi, Restricted replication of herpes simplex virus in human monocyte cultures: role of interferon, *Virology* 130 (1) (1983) 1–9, [https://doi.org/10.1016/0042-6822\(83\)90112-5](https://doi.org/10.1016/0042-6822(83)90112-5).
- [47] F.H.N. Howard, H. Al-Janabi, et al., Nanobugs as drugs: bacterial derived nanomagnets enhance tumor targeting and oncolytic activity of HSV-1 virus, *Small* 18 (2022) 2104763, <https://doi.org/10.1002/smll.202104763>.
- [48] M. Luo, L.K.C. Lee, B. Peng, C.H.J. Choi, W.Y. Tong, N.H. Voelcker, Delivering the promise of gene therapy with nanomedicines in treating central nervous system diseases, *Adv. Sci.* 9 (26) (2022) 2201740, <https://doi.org/10.1002/adv.202201740>.
- [49] L.K.C. Lee, L.I. Leong, Y. Liu, M. Luo, H.Y.E. Chan, C.H.J. Choi, Preclinical nanomedicines for polyglutamine-based neurodegenerative diseases, *Mol. Pharm.* 18 (2) (2021) 610–626, <https://doi.org/10.1021/acs.molpharmaceut.0c00506>.
- [50] B.-Z. Qian, J. Li, H. Zhang, T. Kitamura, J. Zhang, L.R. Campion, E.A. Kaiser, L. A. Snyder, J.W. Pollard, CCL2 recruits inflammatory monocytes to facilitate breast-tumour metastasis, *Nature* 475 (7355) (2011) 222–225, <https://doi.org/10.1038/nature10138>, 8.
- [51] P. Trionfini, E. Romano, et al., Hypoimmunogenic human pluripotent stem cells as a powerful tool for liver regenerative medicine, *Int. J. Mol. Sci.* 24 (2023) 11810, <https://doi.org/10.3390/ijms241411810>.
- [52] T.S. Park, R. Hirday, R. Quinn, S.P. Jacob, R.A. Feldman, D. Bose, R. Sharma, K. Bharti, Differentiation of monocytes and polarized M1/M2 macrophages from human induced pluripotent stem cells, *STAR Protoc.* 5 (1) (2024) 102827, <https://doi.org/10.1016/j.xpro.2023.102827>.
- [53] Y. Xia, G.M. Whitesides, Soft lithography, *Angew. Chem., Int. Ed. Engl.* 37 (1998) 550–575, [https://doi.org/10.1002/\(SICI\)1521-3773\(19980316\)37:5<550::AID-ANGE550>3.0.CO;2-G](https://doi.org/10.1002/(SICI)1521-3773(19980316)37:5<550::AID-ANGE550>3.0.CO;2-G).
- [54] B. Peng, Z. Tong, W.Y. Tong, P.J. Pasic, A. Oddo, Y. Dai, M. Luo, J. Frescene, N. G. Welch, C.D. Easton, H. Thissen, N.H. Voelcker, *In situ* surface modification of microfluidic blood-brain-barriers for improved screening of small molecules and nanoparticles, *ACS Appl. Mater. Interfaces* 12 (51) (2020) 56753–56766, <https://doi.org/10.1021/acsami.0c17102>.
- [55] W.Y. Chan, Y. Ding, J.Y. Tu, Modeling of Non-Newtonian blood flow through a stenosed artery incorporating fluid-structure interaction, *Proc. 7th Bienn. Eng. Math. Appl. Conf. EMAC-2005* (2007) C507–C523, <https://doi.org/10.21914/anzi.2007.1059>.
- [56] S. Micheli, P. Mocellin, M. Sorgato, L. Bova, E. Cimetta, Modeling-based design specifications for microfluidic gradients generators for biomedical applications, *Biochem. Eng. J.* 181 (2022) 108415, <https://doi.org/10.1016/j.bej.2022.108415>.
- [57] V. Zingales, C. Piunti, S. Micheli, E. Cimetta, M.-J. Ruiz, Development of an easy-to-use microfluidic system to assess dynamic exposure to mycotoxins in 3D culture models: evaluation of Ochratoxin A and Patulin cytotoxicity, *Foods* 13 (24) (2024) 4167, <https://doi.org/10.3390/foods13244167>.
- [58] F. Piccinini, AnaSP: a software suite for automatic image analysis of multicellular spheroids, *Comput. Methods Programs Biomed.* 119 (1) (2015) 43–52, <https://doi.org/10.1016/j.cmpb.2015.02.006>.
- [59] B.K. Tischer, J. von Einem, B. Kaufer, N. Osterrieder, Two-step red-mediated recombination for versatile high-efficiency markerless DNA manipulation in *Escherichia coli*, *Biotechniques* 40 (2) (2006) 191–197, <https://doi.org/10.2144/000112096>.
- [60] A. Vitiello, A. Reale, V. Conciatori, A. Vicco, A. Garzino-Demo, G. Palù, C. Parolin, J. von Einem, A. Calistri, Simultaneous expression of different therapeutic genes by infection with multiple oncolytic HSV-1 vectors, *Biomedicines* 12 (2024) 1577, <https://doi.org/10.3390/biomedicines12071577>.
- [61] A.J. Ulmer, H.D. Flad, Discontinuous density gradient separation of human mononuclear leucocytes using Percoll as gradient medium, *J. Immunol. Methods* 30 (1) (1979) 1–10, [https://doi.org/10.1016/0022-1759\(79\)90268-0](https://doi.org/10.1016/0022-1759(79)90268-0).